Received: 11 March 2020 | Revised: 25 May 2020 | Accepted: 26 May 2020
DOI: 10.1002/wcms.1492

ADVANCED REVIEW

WIREs COMPUTATIONAL MOLECULAR SCIENCE WILEY

First-principles dynamics of photoexcited molecules and materials towards a quantum description

Peiwei You[1,2] | **Daqiang Chen**[1,2] | **Chao Lian**[1] | **Cui Zhang**[1,3] | **Sheng Meng**[1,2,3]

[1]Beijing National Laboratory for Condensed Matter Physics and Institute of Physics, Chinese Academy of Sciences, Beijing, China

[2]School of Physical Sciences, University of Chinese Academy of Sciences, Beijing, China

[3]Songshan Lake Materials Laboratory, Dongguan, China

Correspondence
Sheng Meng, School of Physical Sciences, University of Chinese Academy of Sciences, Beijing 100049, China.
Email: smeng@iphy.ac.cn

Funding information
"Strategic Priority Research Program B" of the CAS, Grant/Award Number: XDB330301; Ministry of Science and Technology of the People's Republic of China (MOST), Grant/Award Numbers: 2015CB921001, 2016YFA0300902; NSFC, Grant/Award Numbers: 11774396, 11974400, 11934003, 91850120

Abstract

The past decades have witnessed the success of ground-state density functional theory capturing static electronic properties of various materials. However, for time dependent processes especially those involving excited states, real-time time-dependent density functional theory (rt-TDDFT) and advanced nonadiabatic algorithms are essential, especially for practical simulations of molecules and materials under the occurrence of ultrafast laser field. Here we summarize the recent progresses in developing rt-TDDFT approaches within numerical atomic orbitals and planewave formalisms, as well as the efforts combining rt-TDDFT and ring polymer molecular dynamics to take into account nuclear quantum effects in quantum electronic-nuclear dynamic simulations. Typical applications of first-principles dynamics of excited electronic states including high harmonic generation, charge density wave, photocatalytic water splitting, as well as quantum nuclear motions in ozone and graphene, are presented to demonstrate the features and advantages of these methods. The progresses in method developments and practical applications provide unprecedented insights into nonadiabatic dynamics of excited states in the Ehrenfest scheme and beyond, towards a comprehensive understanding of excited electronic structure, electron–phonon interactions, photoinduced charge transfer and chemical reactions, as well as quantum nuclear motions in excited states.

This article is categorized under:
Electronic Structure Theory > Ab Initio Electronic Structure Methods
Electronic Structure Theory > Density Functional Theory
Molecular and Statistical Mechanics > Molecular Dynamics and Monte-Carlo Methods

KEYWORDS
first principles, nonadiabatic dynamics, nuclear quantum effects, photoexcitation, time dependent density functional theory

1 | INTRODUCTION

Many phenomena such as chemical reactions,[1–3] electron–phonon couplings (EPCs)[4,5] and ultrafast laser-induced dynamics[6–10] stem from atomic-level nonadiabatic dynamics. Herein, traditional Born–Oppenheimer approximation (BOA), which allows us to construct a well-defined potential energy surface (PES), is invalid. In BOA, the electrons and nuclei are decoupled, because the electrons move much faster than nuclei and the nuclei are regarded as "frozen" when considering electronic dynamics. For nonadiabatic dynamics, the coupling between electrons and nuclei cannot be ignored, indicating a breakdown of BOA. To investigate these nonadiabatic dynamics essential for the development of modern science and technology, exact or numerical solutions of time dependent Schrödinger equation (TDSE), especially in the presence of external field, are required. In the past decades, some computational methods aiming at full quantum dynamics have been developed, including multiconfiguration time-dependent Hartree[11,12], variational multi-configurational Gaussian wave packet method,[13] and multiple spawning approaches.[14] However, suffering from high computational costs, these methods are usually limited to small systems containing a few to tens of atoms

Considering classical nuclear approximations, one can remarkably reduce the computational costs corresponding to nuclear degrees of freedom, avoiding the precalculated PES. The mixed quantum–classical dynamics, where some degrees of freedom obey quantum mechanics and others are treated classically, have been rapidly developed in recent years. These approaches including quantum–classical Liouville dynamics,[15,16] nonadiabatic Bohmian dynamics,[17] coupled-trajectories mixed quantum–classical method,[18] fewest-switches surface-hopping algorithm[19,20] (FSSH), and Ehrenfest dynamics,[21–24] enable us to simulate large-scale mixed quantum−classical dynamics of realistic materials at present. It should be noted that ab initio multiple spawning, where the Gaussian functions representing nuclear wave packet are evolved along classical trajectories, can deal with nearly the same size as FSSH.

Here we focus on recent progresses in developing first-principles simulation methods dealing with nonadiabatic excited state dynamics based on Ehrenfest scheme and beyond. In the presence of external field, the electronic evolutions and nuclear motions of the system are strongly coupled, therefore, the BOA is not valid anymore and the time-domain propagation of excited electronic states is required in Ehrenfest schemes. By the way, the treatment of excited state dynamics processes with an explicit external field can also be performed within the Born–Huang representation of the molecular wavefunctions, based on a linear combination of Born–Oppenheimer (time-independent) electronic states. Real-time time-dependent density functional theory (rt-TDDFT), wherein time-dependent Kohn–Sham (TDKS) equations are numerically solved, has been implemented in many software, for example, SALMON,[25] ELK,[26] OCTOPUS,[27] GPAW,[28–30] YAMBO,[31] NWCHEM[32] and so on. Our homemade time dependent ab initio package (TDAP)[22,33] and time dependent ab initio plane wave code (TDAPW) have followed this line of progresses. The main features and some differences of these rt-TDDFT approaches are listed in Table 1. Different technical approaches have been adopted; for example, TDKS equations are solved on real-space grids (RSG) in OCTOPUS and SALMON, and in reciprocal space for the rest of codes. ELK is a full potential augmented planewave (PW) method while TDAPW is based on pseudopotentials and the PW formalism, and TDAP adopts numerical atomic orbital (NAO) basis sets. Generally, parallelization schemes can be efficiently achieved while using RSG but not efficient to deal with extended systems. With a large-scale basis set, PW can provide higher accuracy but limit to relatively smaller systems. The NAO basis

TABLE 1 Some software on rt-TDDFT and their main features

	TDAP	TDAPW	OCTOPUS	ELK	GPAW	YAMBO	NWCHEM	SALMON
Multi-K	√	√	√	√	×	√	×	√
Dipole field	√	√	√	●	√	●	√	√
Vector field	√	√	√	√	×	√	×	√
Berry phase	√	×	×	√	×	√	×	×
MD	√	√	√	×	●	×	●	●
PIMD	√	×	×	×	×	×	×	×
TypeBasis	NAO[2]	PW[3]	RSG[3]	PW[4]	RSG/NAO	RSG	Gaussian	RSG[3]
NumBasis/N_a	10	10^3	10^4	10^5	10^4/10	10^4	10^2	10^4
TimeStep/as	50	50	1	1	10	1	2.5	1

√, realized; ●, realized but problematic; ×, not realized.

requires a small amount of basis set but in some sense sacrifices the computational accuracy, benefiting from calculations of orbital related physical quantities.

Combining the time-domain quantum evolution of electronic states with the classical approximations of nuclear motions, the scheme of Ehrenfest dynamics has been implemented in the OCTOPUS, TDAP, and TDAPW codes. Within the classical-nuclei approximation, nuclei move in the mean field of electronic PES, and forces acting on the nuclei are calculated on-the-fly.

To further consider nuclear quantum effects (NQEs), ring polymer molecular dynamics (RPMD) based on imaginary-time path integral simulations of nuclear trajectory has been introduced.[34,35] Tully et al. have further developed a nonadiabatic method of RPMD implemented with FSSH, but its application is limited by the heavy computational cost if real excited state PES are used. Consequently, we have proposed a new strategy to deal with quantum nuclear motions and time dependent electronic evolutions, for both finite and periodic systems.[36] This newly developed approach, termed ring polymer time-dependent ab initio propagation (RP-TDAP), allows us to capture the NQE in excited state nonadiabatic dynamics and investigate the scenarios beyond Ehrenfest scheme.

In the following sections we limit our attention to first principles rt-TDDFT algorithms implemented with NAOs and PW basis sets, together with the framework of RP-TDAP approach, a full quantum dynamics description for electrons and nuclei. Intriguing applications of these methods are presented in subsequent sections, including strain-induced tunable high harmonic generation (HHG) in monolayer MoS_2,[37] novel photoinduced collective mode and complete inversion of charge density wave (CDW) ordering in 1T-$TiSe_2$,[38,39] photocatalytic water splitting induced by the proton transfer in Au_{20} cluster[40] and the hole transfer process in g-C_3N_4, as well as the quantum evolution of nuclear wave packets in ozone and ultrafast carrier relaxation in graphene.[36] The results establish the feasibility of our approaches and hint for new insights in understanding complex nonadiabatic dynamics of excited states in a full quantum framework.

2 | METHODOLOGY

The Hamiltonian of a combined electronic and nuclear system is defined as

$$\hat{H}_{\mathrm{tot}}(\mathbf{r},\mathbf{R},t)=\hat{T}_{\mathrm{N}}(\mathbf{R})+\hat{H}_{\mathrm{BO}}(\mathbf{r},\mathbf{R})+U_{\mathrm{ext}}(\mathbf{r},\mathbf{R},t), \tag{1}$$

where $\hat{T}_{\mathrm{N}}, \hat{H}_{\mathrm{BO}}$, U_{ext} represent the nuclear kinetic energy, the external potential, and electronic Hamiltonian, respectively; $\mathbf{r}$ and $\mathbf{R}$ are the collective coordinates of electronic positions $\mathbf{r}_i$ and nuclear positions $\mathbf{R}_\alpha$. The electronic Hamiltonian $\hat{H}_{\mathrm{BO}}$ can be expressed as

$$\hat{H}_{\mathrm{BO}}(\mathbf{r},\mathbf{R})=\sum_i\frac{\hat{p}_i^2}{2m}+\sum_{i<j}\frac{e^2}{|\mathbf{r}_i-\mathbf{r}_j|}-\sum_{i,\alpha}\frac{eZ_\alpha}{|\mathbf{r}_i-\mathbf{R}_\alpha|}+\sum_{\alpha,\beta}\frac{Z_\alpha Z_\beta}{|\mathbf{R}_\alpha-\mathbf{R}_\beta|}=\hat{T}_{\mathrm{el}}+V(\mathbf{r},\mathbf{R}). \tag{2}$$

Here the electronic kinetic energy $\hat{T}_{\mathrm{el}}$ is defined as $\sum_i \frac{\hat{p}_i^2}{2m}$, where m is the mass of electrons and p_i is the momentum of ith electron; the rest terms are denoted as $V(\mathbf{r}, \mathbf{R})$, where e and Z_α are the charge of electron and the αth nucleus, respectively. As discussed in References 21,23, the time-dependent self-consistent field formula (TDSCF) can be derived by simplifying the total wavefunction into the product of electronic and nuclear wavefunctions. Therefore, the explicit dependence of electronic wavefunctions on nuclear coordinates is removed and the Berry phase of electronic wavefunctions with respect to nuclear coordinates under the derivation disappears.[41,42] The TDSCF equations under an external field are obtained as the following:

$$i\hbar\frac{\partial}{\partial t}\varphi(\mathbf{r},t)=\left[\hat{T}_{el}+\int d\mathbf{R}\chi^*(\mathbf{R},t)[V(\mathbf{r},\mathbf{R})+U_{\mathrm{ext}}(\mathbf{r},\mathbf{R},t)]\chi(\mathbf{R},t)\right]\varphi(\mathbf{r},t), \tag{3}$$

$$i\hbar\frac{\partial}{\partial t}\chi(\mathbf{R},t)=\left[\hat{T}_N+\int d\mathbf{r}\varphi^*(\mathbf{r},t)\left[\hat{H}_{BO}(\mathbf{r},\mathbf{R})+U_{\mathrm{ext}}(\mathbf{r},\mathbf{R},t)\right]\varphi(\mathbf{r},t)\right]\chi(\mathbf{R},t). \tag{4}$$

Here $\varphi(\mathbf{r}, t)$ and $\chi(\mathbf{R}, t)$ represent electronic and nuclear wavefunctions, respectively; the external field $U_{\text{ext}}(\mathbf{r}, \mathbf{R}, t)$ is introduced. New electronic Hamiltonian can be written as $\hat{H}_{\text{eff}}(\mathbf{r},\mathbf{R},t) = \hat{H}_{\text{BO}}(\mathbf{r},\mathbf{R}) + U_{\text{ext}}(\mathbf{r},\mathbf{R},t)$ and a mean field of electronic states is obtained by:

$$U(\mathbf{R},t) \equiv \int d\mathbf{r}\varphi^{*}(\mathbf{r},t)\hat{H}_{\text{eff}}(\mathbf{r},\mathbf{R},t)\varphi(\mathbf{r},t). \tag{5}$$

At each time step, the mean field acting on the nuclei is calculated based on TDDFT. With classical approximation of nuclei motions,

$$\chi(\mathbf{R},t) \to \sum\nolimits_{\alpha}\delta(\mathbf{R}(t) - \mathbf{R}_{\alpha}(t)), \tag{6}$$

the time dependent electronic equation (Equation (3)) is reduced to:

$$i\hbar\frac{\partial}{\partial t}\varphi(\mathbf{r},t;\mathbf{R}_{\text{t}}) = \hat{H}_{\text{eff}}(\mathbf{r},\mathbf{R},t)\varphi(\mathbf{r},t;\mathbf{R}_{\text{t}}), \tag{7}$$

where the electronic wavefunction is parametrically dependent on the position of classical nuclei. One can also follow other strategies to derive the Ehrenfest dynamics from TDSCF.[21] To simplify the derivation, we use the delta function expression here.

According to the Runge–Gross theorem,[43] one can follow the idea of utilizing an auxiliary system of noninteracting (Kohn–Sham) electrons in density functional theory and deduce Equation (7) into the TDKS equation:

$$i\hbar\frac{\partial}{\partial t}\psi(\mathbf{r},t) = \hat{H}_{\mathbf{KS}}(\mathbf{r},\mathbf{R},t)\psi(\mathbf{r},t), \tag{8}$$

where $\hat{H}_{\mathbf{KS}}(\mathbf{r},\mathbf{R},t) = \hat{T}_{\text{el}} + \sum V_{I}^{local}(\boldsymbol{r}) + \sum V_{I}^{KB} + V^{H}(\mathbf{r},t) + V^{XC}(\mathbf{r},t) + U_{ext}(\mathbf{r},\mathbf{R},t)$ and $\psi(\mathbf{r}, t)$ are the Kohn–Sham orbitals. Here $V_{I}^{local}(\boldsymbol{r})$ and V_{I}^{KB} are the local and Kleinman–Bylander parts of the pseudopotential of atom I, while $V^{H}(\mathbf{r}, t)$ and $V^{XC}(\mathbf{r}, t)$ are the Hartree and exchange-correlation (XC) potentials, respectively. In contrary to the existence of many good XC functionals in density functional theory, fine approximations of time dependent XC functional $V^{XC}(\mathbf{r}, t)$ are still scarce. It is worthy to note that the XC potential in most popular applications is simply approximated by the adiabatic XC potential—the so-called adiabatic approximation. It is shown some absorption spectra calculated from adiabatic local-density approximation are in good agreement with experimental results, indicating the adiabatic approximations can be used in many cases.[44] However, the deficiencies of this approximation include the underestimated quasiparticle gap, lack of excitons and long-range decay of potential, inherited from the drawbacks of adiabatic XC potentials conventionally used. To consider the excitonic interactions in the spectrum, Gross et al. proposed the bootstrap approximation for the XC kernel.[45] It is still on the way to develop generic workable time-dependent XC potentials.

2.1 | rt-TDDFT employing local atomic basis set

Because orbitals are not orthogonal in NAO basis sets, we express the overlap matrix $S_{\mathbf{k}}$ and Hamiltonian $H_{\mathbf{k}}$ at each $\mathbf{k}$ point as:

$$S_{i\alpha,j\beta,\mathbf{k}} = \sum\nolimits_{s}e^{-i\mathbf{k}\cdot\mathbf{R}_{s}}\langle\xi_{i\alpha}(\mathbf{r}+\mathbf{R}_{s}+\mathbf{b}_{i})|\left(\xi_{j\beta}\left(\mathbf{r}+\mathbf{b}_{j}\right)\right), \tag{9}$$

$$H_{i\alpha,j\beta,\mathbf{k}} = \sum\nolimits_{s}e^{-i\mathbf{k}\cdot\mathbf{R}_{s}}\langle\xi_{i\alpha}(\mathbf{r}+\mathbf{R}_{s}+\mathbf{b}_{i})|\left(\hat{H}_{\mathbf{KS}}\right)\xi_{j\beta}\left(\mathbf{r}+\mathbf{b}_{j}\right)\rangle. \tag{10}$$

Here the lattice vectors are denoted as $\mathbf{R}_s$ ($s = 1, 2, 3, \ldots, N$), where N is truncated to form a finite supercell. The postion of atom i is represented by $\mathbf{b}_i$ and the associated NAO is defined as $\xi_{i\alpha}$, where α denotes both the orbital and angular quantum numbers of the atomic states.

To simulate photoinduced excited electronic states, time-dependent electric field $\mathbf{E}(t)$ can be introduced to the Hamiltonian in two different ways: the length gauge and the vector gauge. Within the length gauge, one can involve the effect of electric field $\mathbf{E}(t)$ via $U_{ext}(\mathbf{r}, t)$,

$$U_{ext}(\mathbf{r}, t) = -\mathbf{E}(t)\cdot\mathbf{r}. \tag{11}$$

In this scenario, auxiliary vacuum layers are required in the direction of electric field, otherwise the energy would diverge at the edge of unit cell. Within the vector gauge derived from a gauge transformation,[46,47] the vector potential $\mathbf{A}$ can be written as:

$$\mathbf{A} = -c\int \mathbf{E}dt, \mathbf{E} = -\frac{1}{c}\frac{\partial \mathbf{A}}{\partial t}, \tag{12}$$

leading to the expression of the electronic kinetic energy part in TDKS equation ($\mathbf{k}$ is the momentum in reciprocal space):

$$\hat{T}_{el} = \frac{1}{2m}\left(\hbar\mathbf{k} - \frac{e}{c}\mathbf{A}\right)^2 = \frac{1}{2m}\left(\hbar\mathbf{k} + e\int \mathbf{E}dt\right)^2, \tag{13}$$

which indicates calculations of periodic systems can be performed in the vector gauge scheme.

Now we can obtain the time propagation of the TDKS equation (Equation (8)), at the approximation of time evolution operator using first order Crank–Nicholson scheme[48]:

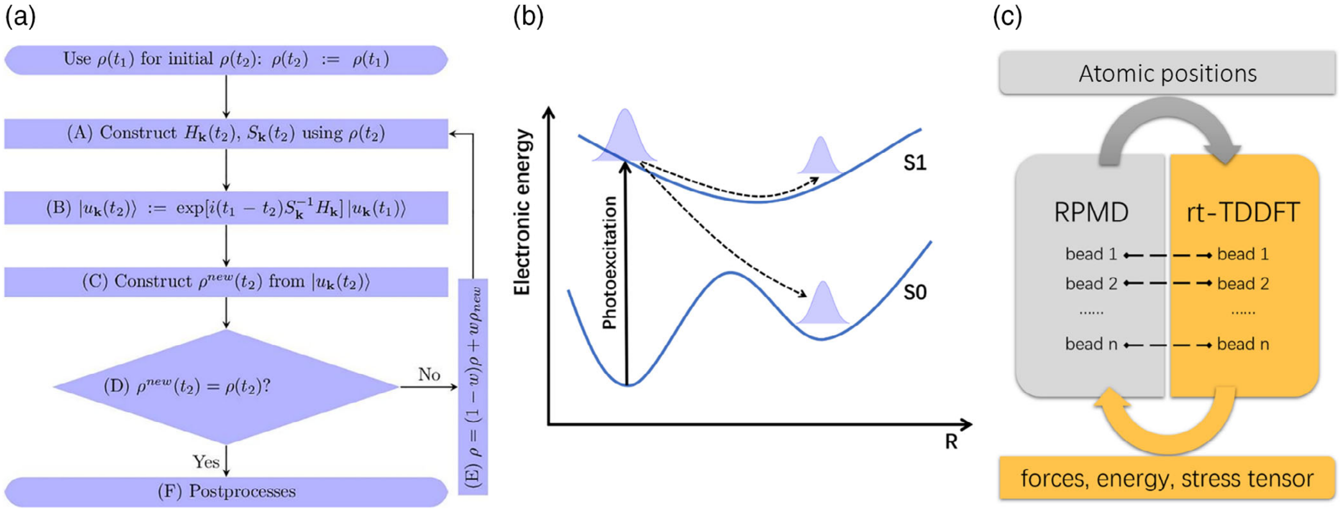

FIGURE 1 . (a) Flowchart of $\mathbf{k}$-resolved algorithm for evolution of electronic system. Here $S_{\mathbf{k}}$, $H_{\mathbf{k}}$, and $u_{n\mathbf{k}}$ are the overlap matrix, Hamiltonian matrix, and TDKS orbitals at $\mathbf{k}$, respectively. (Reprinted with permission from Reference 33. Copyright 2018 Wiley & Sons, Inc.) (b) The scheme of quantum dynamics for electronic and nuclear evolution. At first, electrons are excited by light field and ions move on an excited potential energy surface (S1). Considering the nuclear quantum effect, the wavefunction of nuclei may separate into a few wave packets and exhibit quantum behaviors upon the impact of electronic excitation. (Reprinted with permission from Reference 36. Copyright 2019 IOP Publishing Ltd) (c) Flowchart of RP-TDAP in practical computation. RPMD evolves the atomic positions and rt-TDDFT manages the evaluation of atomic forces. Each bead follows its own electron-nuclear evolution, while all beads are connected by a harmonic spring to neighboring beads (Reprinted with permission from Reference 36. Copyright 2019 IOP Publishing Ltd)

$$|u_{n\mathbf{k}}(\mathbf{r},t_2)\rangle \approx exp\left[-iS_{\mathbf{k}}^{-1}(t')H_{\mathbf{k}}(t')\Delta t\right]|u_{n\mathbf{k}}(\mathbf{r},t_1)\rangle, \tag{14}$$

$$\exp\left[-iS_{\mathbf{k}}^{-1}(t')H_{\mathbf{k}}(t')\Delta t\right] \approx \frac{1-iS_{\mathbf{k}}^{-1}H_{\mathbf{k}}\Delta t/2}{1+iS_{\mathbf{k}}^{-1}H_{\mathbf{k}}\Delta t/2}, \tag{15}$$

where $u_{n\boldsymbol{k}}(\boldsymbol{r}, t) = \psi_{n\boldsymbol{k}}(\boldsymbol{r}, t)e^{-i\boldsymbol{k}\cdot\boldsymbol{r}}$ is the periodic part of Bloch function, and $\Delta t = t_2 - t_1$ is the length of time step. Figure 1a shows the flowchart of real time excited state simulation at a given electronic step.

The motions of nuclei depicted by Equation (4) can be treated within the classical limitation, where the forces applied on the ions are obtained from the following Newton-like equation:

$$-\mathbf{F}_{\alpha}(t) = \int d\mathbf{r}\varphi^{*}(\mathbf{r},t)\nabla_{\alpha}\hat{H}_{\text{eff}}(\mathbf{r},\mathbf{R},t)\varphi(\mathbf{r},t), \tag{16}$$

where $\mathbf{F}_{\alpha}(t)$ is the forces on the nuclei that propagate in the mean field of electronic environment. The expression $-\mathbf{F}_{\alpha}(t) = \nabla_{\alpha}U(\mathbf{R}, t)$ is equivalent to Equation (16), when the $\varphi(\mathbf{r}, t)$ is the solution of Equation (7) but not the eigenstates of $\hat{H}_{\text{eff}}$. Many discussions about the two notations have been reported, and it is shown Equation (16) is a more precise notation, corresponding to a deep insight relevant to the energy conservation.[49–51]

This mean-field nature leads to the limitations of the Ehrenfest dynamics. In the cases where strong nonadiabatic couplings between electrons and nuclei are present, the mean-field dynamics are invalid. Therefore, the Ehrenfest dynamics should be restricted to the dynamics where the nonadiabatic coupling is weak. When the energy difference of two electronic states is large enough, the nonadiabatic coupling leaves the strongly coupled regions. Such applications include absorption spectra, dielectric functions of systems and ultrafast dynamics upon strong laser field in a short period. Another limitation is the deficiency of detailed balance. It is demonstrated the Ehrenfest dynamics deviates from Boltzmann distribution and the final state derived from Ehrenfest dynamics may be controversial.[52]

Taking into account of classical limitation of nuclei, the Ehrenfest-like schemes reduce the computational cost but sacrifice some accuracy, without the need of precomputed PES. From this perspective, NQE, such as quantum tunneling, cannot be included in these dynamics. In comparison to the FSSH method, the Ehrenfest schemes may lose some accuracy in certain circumstances (such as in the region of branching)[53] and cannot retain the detailed balance. However, problems of FSSH, such as overcoherence, can cause unrealistic effects which is reviewed in Reference 54. One can evaluate the nonadiabatic dynamics methods in three aspects: the limitation of time scale, and the size of the system, the accuracy of evolution. In the development of advanced methods, it seems that TDDFT-MD method is a reasonable choice with good compromises between the scale and the accuracy, especially for the extended systems under external electric field, among all other approaches that are currently available.

2.2 | rt-TDDFT employing PW basis set

In addition to NAO basis sets, we also implement the TDDFT approach in the quantum Espresso using a PW basis **G**.[55,56] In the PW basis, the TDKS equation at each **k** point in the Brillouin zone is given by:

$$i\hbar\frac{\partial\psi_{\gamma\mathbf{k}}(\mathbf{G},t)}{\partial t} = \mathcal{H}_{\mathbf{k}}(t)\psi_{\gamma\mathbf{k}}(\mathbf{G},t), \tag{17}$$

where γ denotes the index of TDKS states. $\mathcal{H}_{\mathbf{k}}(t)$ is the Hamiltonian operator represented by the PW basis:

$$\mathcal{H}_{\mathbf{k}}(\mathbf{G},\mathbf{G}',t) = \frac{\hbar^2}{2m}|\mathbf{k}+\mathbf{G}+\mathbf{A}(t)|^2\delta_{\mathbf{G},\mathbf{G}'} + V(\mathbf{G},\mathbf{G}',t). \tag{18}$$

Here $V(\mathbf{G}, \mathbf{G}^{'}, t)$ is the potential energy term, including ion-electron potential, Hartree potential and XC potential, and so on. The $\mathbf{A}(t)$ is the external potential in the velocity gauge, which is denoted:

$$\mathbf{A} = -c\int \mathbf{E}dt, \mathbf{E} = -\frac{1}{c}\frac{\partial \mathbf{A}}{\partial t}. \tag{19}$$

To accelerate computation, the adiabatic basis $\phi_{i\mathbf{k}}(\mathbf{G}, t_1)$ and the eigenstates of the Hamiltonian $\mathcal{H}_{\mathbf{k}}(\mathbf{G},t_1)$ are used to expand TDKS states:

$$\mathcal{H}_{\mathbf{k}}(\mathbf{G},t_1)\,|\,(\phi_{i\mathbf{k}}(\mathbf{G},t_1)) = \epsilon_{i\mathbf{k}}(t_1)\,|\,(\phi_{i\mathbf{k}}(\mathbf{G},t_1)), \tag{20}$$

$$|\left(\psi_{\gamma\mathbf{k}}(\mathbf{G},t)\right) = \sum\nolimits_i c_{i\gamma,\mathbf{k}}(t)\,|\,(\phi_{i\mathbf{k}}(\mathbf{G},t_1)). \tag{21}$$

Here $\epsilon_{i\mathbf{k}}$ is the eigenvalue and i is the band index ($i = 1, 2, 3, \ldots, N_b$), where N_b is the total number of bands. The coefficient $c_{i\gamma,\ \mathbf{k}}(t)$ is $\langle\phi_{i\mathbf{k}}(\mathbf{G}, t_1)\,|\,\psi_{\gamma\mathbf{k}}(\mathbf{G}, t)\rangle$. Typically, the dimension of operator represented in the adiabatic basis ($N_b \times N_b$, $N_b{\sim}10^2$) is usually much less than that in the PW basis ($N_{\mathrm{G}} \times N_{\mathrm{G}}$, $N_{\mathrm{G}}{\sim}10^4$). We notate the Hamiltonian operator represented with the adiabatic basis as H, to distinguish from the Hamiltonian $\mathcal{H}$ represented with the PW basis.

Now by introducing coefficient matrix $C_{\mathbf{k}}(t)$, the TDKS equation can be solved based on the adiabatic basis:

$$H_{\mathbf{k}}(t)C_{\mathbf{k}}(t) = i\hbar\frac{\partial}{\partial t}C_{\mathbf{k}}(t), \tag{22}$$

$$C_{\mathbf{k}}(t) = \begin{pmatrix} c_{11,\mathbf{k}}(t) & c_{12,\mathbf{k}}(t) & \cdots & c_{1N_e,\mathbf{k}}(t) \\ c_{21,\mathbf{k}}(t) & c_{22,\mathbf{k}}(t) & \cdots & c_{2N_e,\mathbf{k}}(t) \\ \vdots & \vdots & \ddots & \vdots \\ c_{N_b1,\mathbf{k}}(t) & c_{N_b2,\mathbf{k}}(t) & \cdots & c_{N_bN_e,\mathbf{k}}(t) \end{pmatrix}, \tag{23}$$

$$H_{\mathbf{k}}(t) = \begin{pmatrix} h_{11,\mathbf{k}}(t) & h_{12,\mathbf{k}}(t) & \cdots & h_{1N_b,\mathbf{k}}(t) \\ h_{21,\mathbf{k}}(t) & h_{22,\mathbf{k}}(t) & \cdots & h_{2N_b,\mathbf{k}}(t) \\ \vdots & \vdots & \ddots & \vdots \\ h_{N_b1,\mathbf{k}}(t) & h_{N_b2,\mathbf{k}}(t) & \cdots & h_{N_bN_b,\mathbf{k}}(t) \end{pmatrix}. \tag{24}$$

By considering Δt is quite small in real simulations ($\Delta t = t_2 - t_1$), one can approximate the time evolution of the Hamiltonian as a linear variation within $[t_1, t_2]$[57,58]:

$$H_{\mathbf{k}}(t) \approx H_{\mathbf{k}}(t_1) + \frac{t - t_1}{t_2 - t_1}[H_{\mathbf{k}}(t_2) - H_{\mathbf{k}}(t_1)]. \tag{25}$$

Through unitary transformation, $H_{\mathbf{k}}(t_2)$ represented in the adiabatic basis $\phi_{i\mathbf{k}}(\mathbf{G}, t_1)$ can be derived from $H'_{\mathbf{k}}(t_2)$ constructed by the adiabatic basis $\phi_{i\mathbf{k}}(\mathbf{G}, t_2)$:

$$H_{\mathbf{k}}(t_2) = S_{\mathbf{k}}^{-1}H'_{\mathbf{k}}(t_2)S_{\mathbf{k}}, \tag{26}$$

$$S_{ij,\mathbf{k}}(t_1,t_2) = (\phi_{i\mathbf{k}}(\mathbf{G},t_2))\,|\,\left(\phi_{\ j\mathbf{k}}(\mathbf{G},t_1)\right). \tag{27}$$

Here the matrix elements of $H'_{\mathbf{k}}(t_2)$ is expressed as:

$$h'_{ij,\mathbf{k}}(\mathrm{t}_2) = (\phi_{i\mathbf{k}}(\mathbf{G},t_2))|\mathcal{H}_{\mathbf{k}}(\mathbf{G},t_2)|\left(\phi_{\ j\mathbf{k}}(\mathbf{G},t_2)\right) = \delta_{ij}\epsilon_{i,\mathbf{k}}(t_2), \tag{28}$$

where $\phi_{i\mathbf{k}}(\mathbf{G}, t_2)$ can be obtained by diagonalizing $\mathcal{H}_{\mathbf{k}}(\mathbf{G},t_2)$ and solving Equation (20) at t_2.

As for the coefficient matrix $C_{\mathbf{k}}(t)$ in Equation (22), its time propagator can be acquired in the form of:

$$C_{\mathbf{k}}(t_2) = U_{\mathbf{k}}(t_2, t_1) C_{\mathbf{k}}(t_1), \tag{29}$$

where $U_{\mathbf{k}}(t_2, t_1)$ is the evolution operator. According to the Crank–Nicholson scheme, when time step dt is sufficiently small and $dtH \ll 1$, the approximate expression of $U_{\mathbf{k}}(t_2, t_1)$ is

$$U_{\mathbf{k}}(t_2, t_1) \approx \prod\nolimits_{s=0}^{N_t - 1} \frac{1 - i\hbar H_{\mathbf{k}}\left(t_s + \frac{dt}{2}\right) dt/2}{1 + i\hbar H_{\mathbf{k}}\left(t_s + \frac{dt}{2}\right) dt/2}, \tag{30}$$

where the $t_s = t_1 + sdt$ and $dt = \Delta t / N_t \sim 0.1$ attosecond. $H_{\mathbf{k}}(t_s + dt/2)$ in the equation can be obtained from Equations (25)–(28). This strategy allows us to capture the time propagation of electronic states with a relatively large time step $\Delta t \sim 0.2$ fs and avoid the divergence of electronic state during its time evolution. By solving time dependent TDKS equation using the PW basis sets, the time propagation of the electronic state is determined and the forces acting on the nuclei can be computed by Equation (16), within classical approximation on nuclear motions.

2.3 | Advanced full quantum dynamics approach

In this section, we discuss a practical computational approach combining rt-TDDFT with RPMD to describe quantum motions of both electrons and nuclei, as schematically shown in Figure 1b. Generalizing exact path integral molecular dynamics (MD) for static equilibrium properties, RPMD is a simple approximate technique to treat real-time dynamics[59] and has been used to calculate chemical reaction rates[60] and the quantum diffusion of liquid water.[61] The RPMD approach provides quantum statistics and semi-classical dynamics descriptions by constructing a fictitious polymer for the original system.[34] The polymer is comprised of n replicas (beads) of the real poly-atomic system and each bead of the same atom is linked by harmonic spring interactions, the elastic constant of which is proportional to the square of temperature, $k \equiv M\omega_n^2 = M\left(\frac{nk_BT}{\hbar}\right)^2$. By applying the concept of RPMD, the nuclear Hamiltonian can be expressed as:

$$H_n(\mathbf{p}, \mathbf{R}, t) = \sum\nolimits_{j=1}^{n} \left[\frac{\left|\mathbf{p}_j\right|^2}{2M} + \frac{1}{2} M\omega_n^2 \left|\mathbf{R}_j - \mathbf{R}_{j-1}\right|^2 \right] + \sum\nolimits_{j=1}^{n} U_j(\mathbf{R}, t). \tag{31}$$

Here $H_n(\mathbf{p}, \mathbf{R}, t)$ represents the Hamiltonian of n-bead ring polymers and $U(\mathbf{R}, t)$ is the potential determined by electronic states; M and ω_n are the mass of nuclei and the frequency of the spring linking n-bead ring polymers, respectively. In this scheme, the nuclear wavefunction $\chi(\mathbf{R}, t)$ is sampled by a sufficient number of classical beads. Nuclear motions are solved from:

$$\dot{\mathbf{p}}_j = -\frac{\partial H_n(\mathbf{p}, \mathbf{R}, t)}{\partial \mathbf{R}_j}, \tag{32}$$

$$\dot{\mathbf{R}}_j = \frac{\partial H_n(\mathbf{p}, \mathbf{R}, t)}{\partial \mathbf{p}_j}. \tag{33}$$

The TDSCF equation of electron Equation (3) can also be degraded into rt-TDDFT equation for each bead:

$$i\hbar \frac{\partial}{\partial t} \varphi_j(\mathbf{r}, t, \mathbf{R_t}) = \hat{H}_{\text{eff}}^{j}(\mathbf{r}, \mathbf{R_t}, t) \varphi_j(\mathbf{r}, t, \mathbf{R_t}). \tag{34}$$

In practice, a finite number of classical beads are chosen to sample the path-integral during the RPMD simulations. To get the thermal equilibrium state at the beginning, the initial sampling from RPMD is always necessary. Although certain classical limits are applied in both Equations (3) and (4), quantum nuclear effects are elegantly treated to a certain degree for both nuclei evolution and electronic propagation, attributed to the fundamental principles of RPMD method. According to the isomorphism between a quantum particle and classical ring polymer, the beads in real-time dynamics can be regarded as the possibly existing state of a quantum particle. With the sufficient number of beads adopted in the simulation, the PES of both ground and excited states can be sampled properly and the influence of problematic bead connections is negligible, leading to a more accurate quantum description. Overall, if information on all beads is collected, this combination presents a certain extent of quantum nuclear effects to both nuclei evolution and electronic propagation. In this sense, the limitation should still be related to the mean-field nature of Ehrenfest scheme. If the energy difference between excited states and ground state is large enough and the nuclei subsystem approximately reaches quasiequilibrium, our method can provide efficient sampling for both the excited state and ground state, in some sense improving the mean-field nature of Ehrenfest scheme. For strongly coupled systems, whether the method can improve the entangled electron-nuclear dynamics remains an open question.

We denote the approach introduced above as the RP-TDAP method, a practical computational scheme to describe the quantum mechanical behavior of both electrons and nuclei by combining rt-TDDFT and RPMD methods. In our RP-TDAP method, the nuclear motion is solved within RPMD scheme using Equations (32) and (33) and the electronic state propagation is derived from Equation (34). The external potential required in RPMD calculations is obtained from the electronic dynamics calculations within rt-TDDFT framework. In such quantum electronic-nuclear dynamics simulations, rt-TDDFT calculations provide the information of ionic forces, electronic energy and stress tensor, while RPMD deals with the evolution of atomic positions and velocities.[62,63] All these quantities are time-dependent and each bead in RPMD must follow the constraints from the previous step. Computational flowchart of the RP-TDAP method is demonstrated in Figure 1c.

3 | APPLICATIONS

Below we present a few examples employing the first-principles approaches introduced above, to explore the electronic-nuclear dynamics of finite and extended systems under intense photoexcitation.

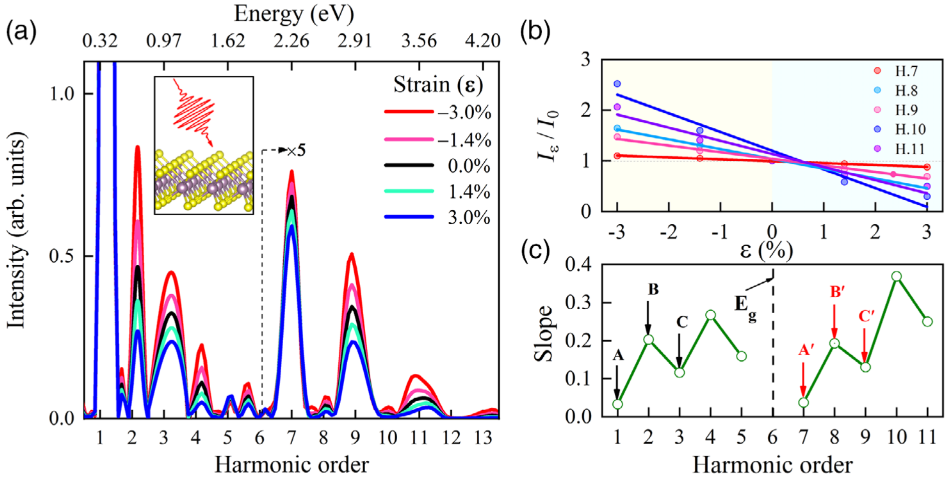

FIGURE 2 . Strain-dependent HHG yield for different harmonics of 1L-MoS_2. (a) Evolution of the normalized HHG spectrum under tensile and compressive strain. (b) The relative change in HHG intensity as a function of strain for representative harmonics (colored dots) and the linear fit (solid lines). (c) Applying the same method to all harmonics, the absolute value of the slope changes nearly periodically. Black and red arrows labeled as X and X′ (X = A, B, …) denote the harmonics in the first and second cycle (Reprinted with permission from Reference 37. Copyright 2019 American Physical Society)

3.1 | High harmonic generation in MoS_2

In the ultrafast regime, attosecond pulses have been developed and employed to track processes in attosecond time-resolved measurements for years,[64–66] owing to the nonlinear effect of HHG. HHG can be explained by two different mechanisms, intraband and interband transitions, respectively. However, the relative contributions and modulation of these two mechanisms are still lack of interpretation.[67,68] Here we present our findings on the high sensitivity of HHG when uniaxial strain is applied in monolayer MoS_2, based on rt-TDDFT simulations.[37] Details of calculating HHG spectrum are shown in References 37,69.

Besides some optical modulation methods, one simple and maneuverable way to manipulate the HHG is applying strain to the host material. To investigate the influence of structural deformation on HHG in MoS_2, we calculate the HHG yields as a function of uniaxial strain, shown in Figure 2a. Under a compressive strain ($\varepsilon < 0$) that only causes up to 3% change in the lattice constant, the yields for all HHG orders are enhanced by ~10 to ~150%. On the contrary, the HHG intensity is reduced with a lower rate when applying the enlarged tensile strain. The sensitivity of HHG in response to small structural variation of MoS_2 shown here indicates that the HHG yields can be continuously tuned by strain and they are more sensitive to the compressive strain than the tensile one.

Furthermore, it is noticed that the strain manipulation plays different impact on HHG with respect to harmonic orders. We show the relative change in HHG intensity I_ε/I_0 (I_ε and I_0 are the HHG yields with and without strain, respectively) in Figure 2b. A nearly linear dependence on strain is found, with the slopes of fitted lines varying with respect to the harmonic orders. We compare the absolute values of slope corresponding to each order, and notice that the slopes of even harmonics are generally larger than that of the odd ones, as shown in Figure 2c.

The results can be interpreted by intraband and interband transitions. Under the compressive strain, the enhancement of intraband contributions can be described by flatter band dispersion and Berry curvature, resulting in enhanced harmonic emission. The picture is that flatter band dispersion and Berry curvature are caused by the higher density of excited carriers from interband transitions, which thus increase the intraband contributions. This analysis of strain-induced band dynamics in monolayer MoS_2 reveals a cooperative effect of intraband and interband excitons on the HHG yields, and that the contributions of intraband dynamics dominate the HHG spectra morphology whereas the interband interactions are indispensable in modulating the HHG emission.

3.2 | Charge density wave

Interplays among electrons, phonons, and spins lead to tremendous interesting properties and phenomena in quantum materials. CDW material is one of the intriguing quantum systems, where electron and phonon degrees of freedom are strongly coupled. Laser-induced phase dynamics in CDW materials have been investigated recently in experiments.[9,70–75] Using the state-of-the-art rt-TDDFT MD, we are able to simulate and probe the laser-induced CDW states and dynamics in a variety of typical CDW materials (e.g., 1T-TaS_2 and 1T-$TiSe_2$).

3.2.1 | Laser-induced dynamics in 1T-TaS_2

Ultrafast laser-induced dynamics in 1T-TaS_2 have been widely studied in experiments recently[70,71,73]; however, the microscopic mechanism concerning how electronic modulations and atomic motions are coupled remains unclear. By means of first principles nonadiabatic MD simulations, we present the intrinsic electron-nuclei coupled dynamics in 1T-TaS_2. Under high laser irradiation, we find a laser-induced new collective mode, with distinctive electronic properties from the normal CDW state.[38]

Photoinduced ultrafast dynamics in 1T-TaS_2 with different levels of photoexcitation are shown in Figure 3. At a low laser intensity of $\eta = 0.64\%$ (η is the ratio of valence electrons pumped into conduction bands by laser), atoms of 1T-TaS_2 oscillate around their equilibrium positions with minor fluctuations, characterized by an oscillating root-mean-square displacement (RMSD) and the lattice distribution retains the feature of "star of David" (SD) pattern (low temperature C state). When applying a stronger light intensity of $\eta = 1.28\%$, melting of the CDW state is observed and the SD pattern is destroyed at ~250 fs with the value of RMSD linearly increasing and reaching 0.25 Å at ~440 fs. We also notice that temperature rises from 10 to 103 K after 100 fs (as shown in Figure 3c), as a result of the energy transfer from electronic orbitals to the kinetic energy of the lattice subsystem. However, we also notice that in 1T-TaS_2, such a

FIGURE 3 . Time evolution of atomic structures of bulk 1T-TaS_2 under different photoexcitation. (a) Snapshots of time-dependent atomic structures for $\eta = 0.64\%$, $\eta = 1.28\%$, and $\eta = 1.92\%$ at 0, 250, 480, and 840 fs after photoexcitation, respectively. (b) Evolution of RMSD under three laser intensities (black line, $\eta = 0.64\%$; purple line, $\eta = 1.28\%$; red line, $\eta = 1.92\%$). (c) Corresponding evolution of the ionic temperatures calculated from the kinetic energy of all ions at different times (Reprinted with permission from Reference 38. Copyright 2019 American Chemical Society)

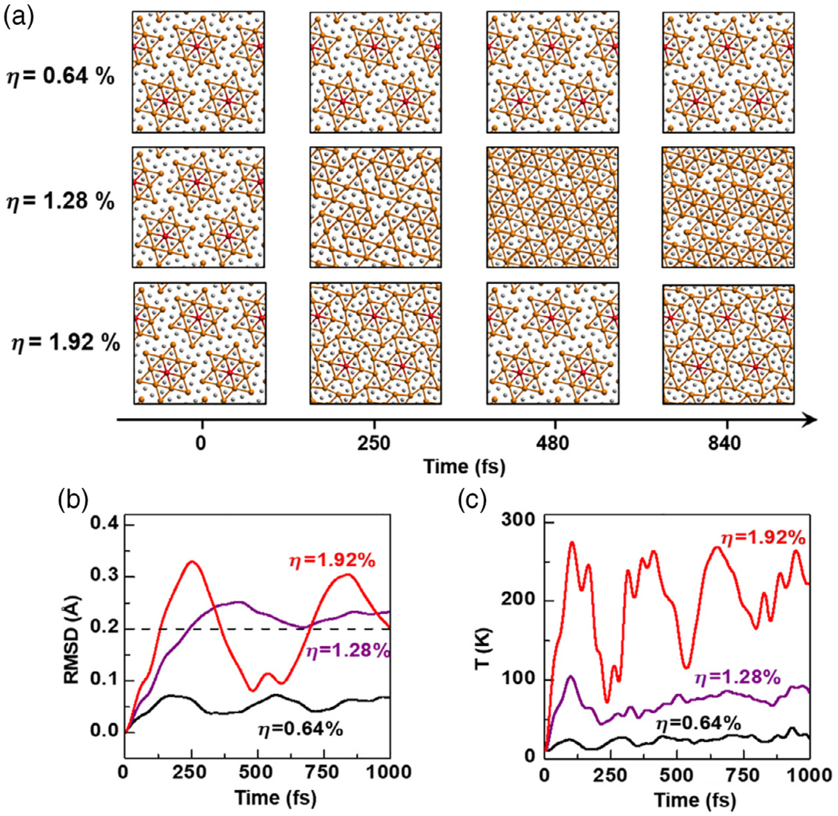

400 K temperature is much lower than the typical thermal melting temperature of CDW, implying the ultrafast CDW melting is not resulted by only lattice thermal effect but with a nature of photoinduced electronic-nuclear property.

For an even stronger laser intensity of $\eta = 1.92\%$, photoinduced phase dynamics exhibits a distinctive electron-nuclei dynamic where the SD collapses at ~250 fs to form new orders and a new transient metallic state (referred to as M state) is generated subsequently. The corresponding RMSD shows an oscillation with a period of 480 fs and reaches 0.32 Å in coordinate with the appearance of M state at ~250 fs. When the RMSD swings down to 0.1 Å at ~480 fs, the SD pattern in the atomic structure is restored.

Therefore, with first principles rt-TDDFT MD simulations, we reveal a collective mode in 1T-TaS_2 induced by photo-doping with a strong laser intensity, where the ultrafast dynamic of CDW state has been proven to be a nonthermal process and cannot be interpreted by hot electron model[70,71] because of the lack of electron–electron scatterings. Capturing the intrinsic properties of photoinduced electronic-nuclear dynamics in 1T-TaS_2, we show a deep perspective for the formation and excitation of CDW in 1T-TaS_2, and these results help us to understand a wide range of laser-induced phenomena in CDW materials. In fact, the simulations related to the EPC, such as CDW dynamics, present reasonable results compared with experimental data, despite that the Ehrenfest scheme is not a rigorous treatment for EPC.

3.2.2 | Self-amplified exciton–phonon dynamics in $TiSe_2$

Which forces are responsible for the formation of CDW in $TiSe_2$ has been debated over years. The major disagreement between the two mechanisms previously proposed: electron–EPC and excitonic paring, lies on the explicit roles of periodic lattice distortions (PLD) in forming the CDW. We adopt the newly developed rt-TDDFT method to perform quantum photoexcitation simulation of $TiSe_2$ under laser pulses, in order to specify a detailed atomic mechanism for the ultrafast CDW dynamics.[39]

Upon laser irradiation, a breakdown of the CDW order induced by bonding–antibonding electronic transition is observed, which then triggers an antiparallel nuclear motion to the original direction of PLD in $TiSe_2$.

To address the electron-lattice dynamics, we first evaluate the dynamical PES from the simulations. Since the total energy is conserved, $E_{tot}(t) = E_p(t) + E_{kin}(t) + E_{kout}(t)$ (here $E_p(t)$, $E_{kin}(t)$, and $E_{kout}(t)$ are the potential energy, in-plane kinetic energy of atoms, and out-of-plane kinetic energy of atoms, respectively), we use $-E_{kin}(t)$ to represent the dynamical PES for in-plane PLD motions and $-E_{kout}(t)$ to characterize energy changes introduced by the trivial out-of-plane A_{1g} mode. We observe that in the first 20 fs, electrons are excited by the laser pulses from the bonding state to the antibonding state, leading to the rise in the potential energy. During 20–300 fs, the dynamical potential energy decreases as a result of the in-plane PLD movements, while the out-of-plane A_{1g} mode also causes a trivial energy oscillation. The crystal structure with the opposite PLD is formed, along with dramatic changes in the non-equilibrium electronic band structure. At about 300 fs, the fully inversion of PLD motion is completed and dynamical PES falls into a local minimum, implying a new quasiequilibrium state with an equivalent symmetry from the original state.

We note that the weakened CDW directly induced by laser excitation is not the only driving force for the PLD inversion; instead, we propose the atomic mechanism where electron dynamics and lattice distortion are facilitated with each other in the CDW dynamics after initial excitation. Through analyzing the time-dependent electronic band structure along Γ-M, we show the ionic movements play a critical impact on the electronic structure, which is in excellent agreement with experimental measurements. Thus, the self-amplified atomic mechanism is identified as the following process: the decrease in the PLD → the decrease in the band gap → the decrease in the energy of photocarriers → the further decrease in PLD.

Based on above analysis, we propose an entangled electron-photon mechanism for charge ordering in $TiSe_2$ that both exciton pairing and the EPC contribute to the PLD/CDW formation within different timescales: the initialization of the formation of CDW is caused by exciton pairing within 20 fs and subsequently dynamics are facilitated by the EPC through a self-amplification process, as shown in Figure 4.

3.3 | Photocatalytic water splitting

Hydrogen production from photocatalytic water splitting provides a promising way to harvest solar energy and gain clean renewable energy sources.[76–78] Extensive efforts have been directed to the development of efficient and stable photocatalytic materials and the understanding of microscopic mechanisms behind water splitting reactions.[77,79–81] The atomic and electronic properties in complex photocatalytic systems are intertwined, and therefore EPC and nonadiabatic dynamics process play critical roles in charge transfer and nuclear motions. With recent advances in sophisticated theories and codes for excitedstate properties and dynamics,[33] the ability to model and simulate photoexcitation reaction and process has been rapidly increased. Here we present our studies on the photoinduced water splitting processes on gold nanoparticles (Au_{20}) and graphitic carbon nitride ($g-C_3N_4$).

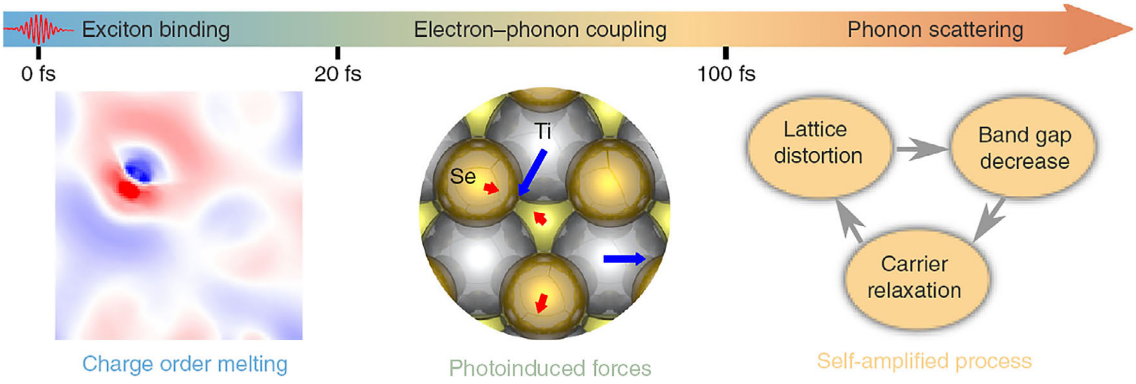

FIGURE 4 Schematic of atomic processes in photoexcited 1T-$TiSe_2$. The laser pulse melts charge order within 20 fs, producing the forces that trigger the ionic movements. The self-amplified dynamics is assisted by electron–phonon couplings after initial excitation (Reprinted with permission from Reference 39. Copyright 2019 Springer Nature)

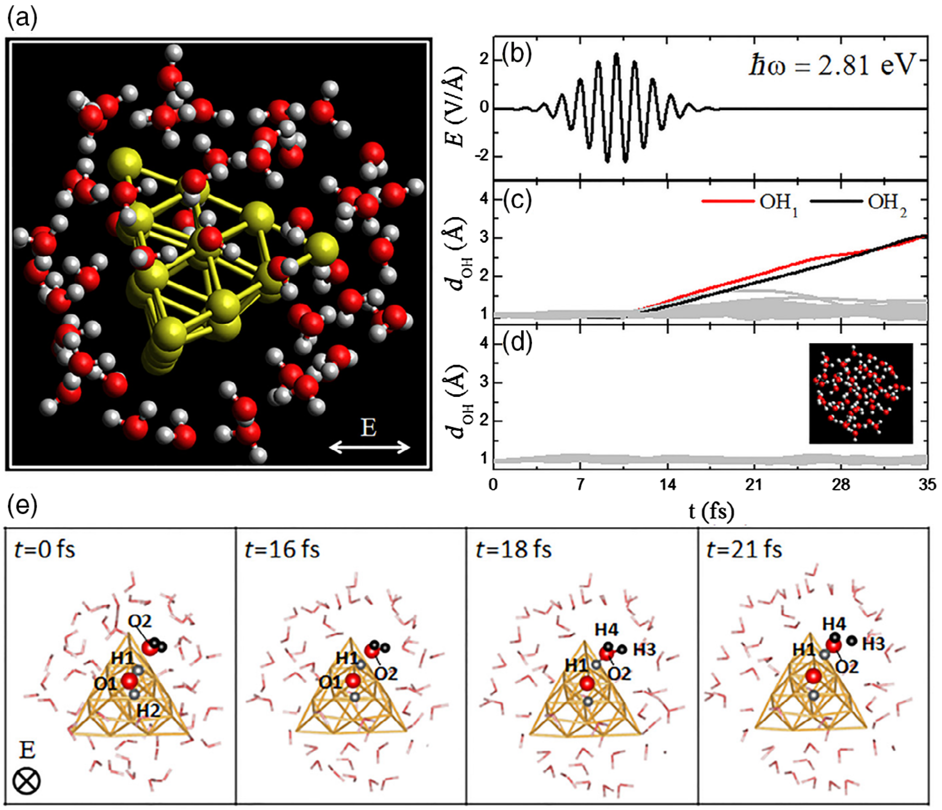

FIGURE 5 (a) Snapshot of the Au_{20} cluster in water, where yellow, red, and gray spheres represent gold, oxygen, and hydrogen atoms, respectively. The arrow denotes polarization direction of the laser field. (b) Time evolution of the laser field with field strength $E_{max} = 2.3$ V/Å and frequency $\hbar\omega = 2.81$ eV. Under this laser pulse, time-evolved O—H bond length d_{OH} of all water molecules with (c) and without (d) Au_{20} cluster are shown. (e) Atomic configurations at time $t = 0$, 16, 18, and 21 fs (Reprinted with permission from Reference 40. Copyright 2018 American Chemical Society)

3.3.1 | Photocatalytic water splitting on Au_{20} cluster

Scientists have observed the direct water splitting when using plasmonic metal nanostructures under irradiation and this decomposition is induced by hot electrons injection from plasmonic metal particles to water molecules, avoiding of the Schottky barrier in the semiconductor–metal co-catalyst systems.[82–84] Good stability and strong catalytic activity of gold nanoparticles make them suitable for catalytic applications.[85] The Au_{20} nanocluster, possessing a unique tetrahedral structure with a high surface area and large fraction of corner sites, provides convenient catalytic sites for water molecule to bind and split.[40] It has been found that field enhancement (FE) near the nanostructure and electron transfer to foreign molecules by nonradiative plasmon decay lead to the high catalytic activity of plasmonic metal clusters.[86,87] However, the dominant mechanism to maximize plasmon-induced photoreaction rates still remains as an open question.

We carry out ab initio rt-TDDFT simulations of laser-irradiated Au_{20} embedded in liquid water,[40,88] as shown in Figure 5. The model system and laser envelope are displayed in Figure 5a,b, respectively. In response to the Gaussian laser pulse of strength up to 2.3 V/Å, we present the dynamical water dissociation process on Au_{20} cluster. In the initial time period from 0 to 10 fs, all O—H bonds oscillate. Due to the emergence of laser pulse, two broken O—H bonds from two separate water molecules are identified. And the bond lengths $d_{OH1} = 1.07$ Å ($d_{OH2} = 0.97$ Å) at $t = 10$ fs increases to 3.11 Å (3.09 Å) at $t = 35$ fs, respectively. That is, two water molecules split into hydroxyl groups (OH) and hydrogen atoms within 35 fs. The water dissociation process is promoted by Au_{20} cluster, in contrast to the case of pure water liquid where no dissociation is observed under the same laser irradiation and timescale, as compared in Figure 5c,d. And we also illustrate the water dissociation process is supported by rapid proton transport due to a Grotthuss-like mechanism,[89] forming hydronium ions (Figure 5e).

We characterize the influence of FE and hot electron transfer for the water splitting reactions assisted by Au_{20} cluster. The dependence of the number of dissociated OH bonds in water on the laser intensity and frequency suggests that the splitting reactions are induced by plasmon. By analyzing the FE spectra displayed in different position around Au_{20} cluster, we find position-dependent FE and reaction rate, where the two quantities have a good correlation. On the other hand, electron transfer from Au_{20} cluster to anti-bonding orbital of water is also revealed by the time-evolved charge density, but it has a weak correlation to water splitting reaction rate. We identify that the water splitting process

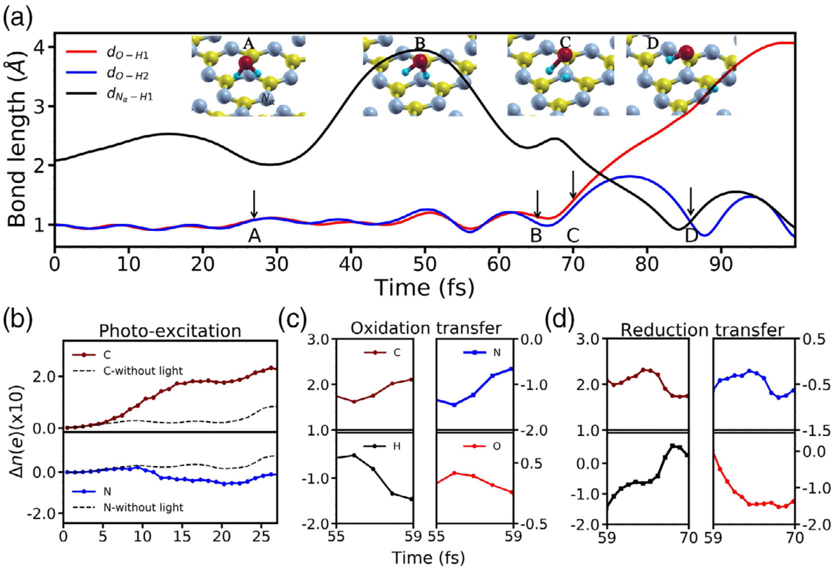

FIGURE 6 (a) Time evolved O—H bond length in single water splitting and four typical snapshots (27, 65, 70, and 86 fs) in the first-principles dynamics. (b) The evolutions of electrons numbers on each species by Hirshfeld charge analysis in 0–27 fs. (c) 55–59 fs. (d) 59–70 fs. We treat the initial state as a zero-electron state and scale the results 10 times, defining this 10-fold charge as pseudo electron

is primarily induced by plasmon-induced FE, while the commonly assumed electron transfer plays a less important role.

3.3.2 | Photocatalytic water splitting on g-C_3N_4

Traditional catalytic materials usually contain metal elements. Metal-free g-C_3N_4, as a potential efficient photocatalyst, exhibits high chemical and thermal stability, inexpensive, and nontoxic nature.[81,90–92] Owing to relatively low hydrogen production, many efforts have been made to improve the photocatalytic efficiency of g-C_3N_4, such as sulfur doping[93,94] and carbon dots embedding.[91] To boost the efficiency and design better photocatalysis, a comprehensive understanding of the microscopic mechanism and electron dynamics of water splitting reaction in g-C_3N_4 is essential, but remain absent. Here we report rt-TDDFT MD simulations of water photocatalytic splitting process on g-C_3N_4. Time evolution of charge transfer process can be directly revealed from our first-principles simulations.

Dynamic processes of single water splitting on g-C_3N_4, irradiated by a laser field with a photon energy of 3.1 eV and an intensity of 0.1 V/Å, are shown in Figure 6. In the first photoexcitation time period of 27 fs, water adsorption structure remains stable, accompanied by electrons excited from nitrogen to carbon atoms in g-C_3N_4. The oxidation transfer occurs during 55–59 fs involving a large proportion of electron injected from water molecule to nitrogen atom and a small portion to carbon, with no obvious change in OH bond length of water. When the system evolves into the reduction transfer period, electrons transfer back from g-C_3N_4 to water molecule together with the initiation of OH bond dissociation. Electron excitation from nitrogen to carbon induces a hole transfer from water to nitrogen, leading to the bond breaking of the water molecule. It suggests a three-step mechanism for the photocatalytic water splitting dynamics in g-C_3N_4, that is also identified in the complex solid–liquid interfacial environments. Different from traditional scheme,[77,95] hole transfer plays a key role in the nonadiabatic photocatalytic process and dominates the water splitting reaction on g-C_3N_4.

3.4 | Quantum electronic-nuclear dynamics

As discussed in the introduction part, one advanced progress in studying quantum dynamics from first principles is the development of a practical computational scheme combining rt-TDDFT and RPMD approaches (RP-TDAP), which can treat quantum nuclear effects going beyond the Ehrenfest dynamics. This advanced method has been applied to both finite (i.e., ozone molecule) and periodic (i.e., graphene sheet) systems and successfully reveals unique electronic and nuclear quantum features upon photoexcitation, which cannot be captured in simulations with a classical atomic trajectory.

FIGURE 7 (a) Atomic configurations of ozone in the normal and cyclic states. (b) The number of excited electrons in each bead of ozone molecule as a function of time at 20 K. (c) Temporal distance of three oxygen atoms in each bead at 20 K. We separate all beads into normal (blue) and cyclic states (red), according to a geometrical criterion (Reprinted with permission from Reference 36. Copyright 2019 IOP Publishing Ltd)

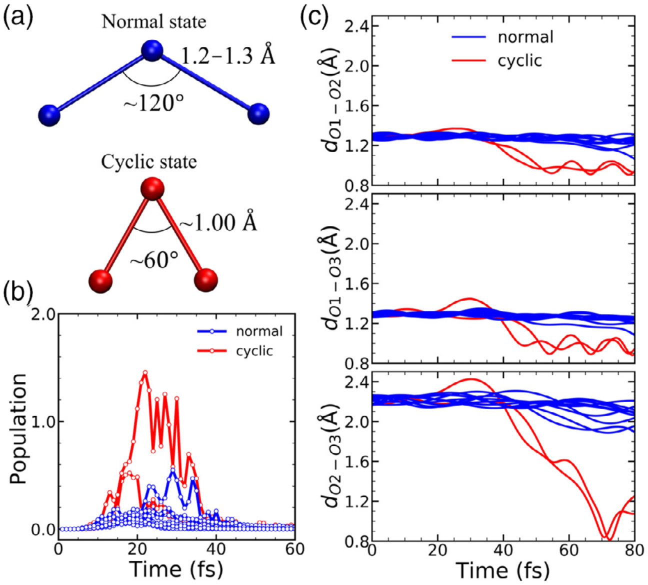

3.4.1 | Nuclear wave packet splitting in ozone

We first present an example that the quantum splitting of nuclear motions are found in ozone molecule under a strong laser excitation when NQEs are considered. The ozone molecule is equilibrated by a standard RPMD simulation carried out in canonical (NVT) ensemble at 20 K for 2 ps, followed by the RP-TDAP simulations performed on the ozone irradiated by an ultraviolet light whose photon energy is 8.75 eV. The direction of the laser field is parallel to the major transition dipole moment of ozone,[96] and the intensity is 0.25 V/Å with a full width at half maximum of 12 fs.

Two local minima structures of ozone, the normal ground state and the cyclic state, have been identified with an energy difference of ~1.3 eV.[97] As shown in Figure 7a, the normal state is defined by the structure feature that O—O bond lengths are between 1.2 and 1.3 Å with an angle around 120°, while the cyclic state is identified by the equilateral structure that O—O distance is ~1.0 Å. Under the excitation of laser at a low temperature of 20 K, the ozone molecule is found to evolve into two distinct configurations, revealed by the difference of the number of excited electrons in each bead and the variance of the distances between beads with time, as shown in Figure 7b,c. According to the geometry criterion in Figure 7a, we separate the beads into the normal and cyclic types based on the structure features of irradiated ozone at 70 fs. During the photoinduction process, the excited beads start splitting into two types of states from ~20 fs, right after the peak time of laser field, and the equilateral cyclic structures are formed at ~70 fs. The excitation population of the beads developing into the cyclic form is five times larger than that of beads remaining in the normal state. It indicates that the high amount of electron excitations is the driving force of the bead state splitting. The radius of gyration, representing the spread of quantum wave packet of nuclei, maintains almost constant for the beads in the normal state during the whole photoexcitation process, indicating a localized wave packet close to the centroid. Instead, the radius of gyration for the beads induced into the cyclic form begins increasing at the end of laser pulse, suggesting the formation of delocalized wave packets away from the centroid.

In response to the photoexcitation, individual beads in ozone end up in two distinct states, arising from different quantum nuclear configurations sampled by the RPMD calculations before the state splitting. By including NQE in rt-TDDFT dynamics simulations, specific feature of quantum nuclear wave packet splitting in ozone during the photoexcitation is captured, that is hardly revealed from the averaged nuclear trajectory along the mixing PES in conventional Ehrenfest dynamics.

3.4.2 | Ultrafast carrier dynamics in graphene

Ultrafast dynamics of photocarriers in graphene has attracted much attention,[7,98–101] attributed to the high mobility and potential high-tech applications of Dirac carriers. For example, recent photoelectron spectroscopy measurements suggest a sequence of three stages within 50 fs for the carrier transfer process in graphene: photo-absorption process

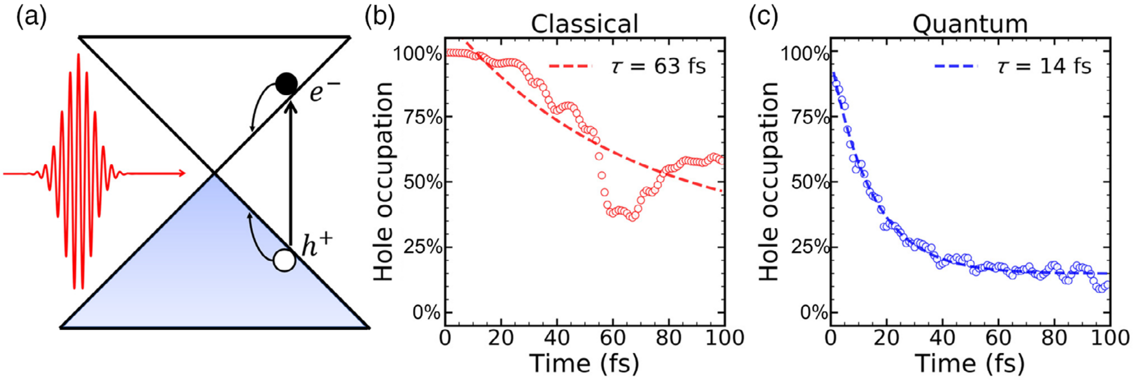

FIGURE 8 (a) Schematic diagram of the photoinduced electron–hole excitation and relaxation processes. The electron hole occupation numbers of graphene as a function of time with the classical and quantum treatments of nuclear motion are shown in (b) and (c), respectively. Dashed lines are the exponential fitting to the hole occupation number (Reprinted with permission from Reference 36. Copyright 2019 IOP Publishing Ltd)

(<8 fs), momentum redistribution (∼10–22 fs) and hot Fermi-Dirac distribution.[10] Electron–electron and electron–phonon scatterings are believed to control such photoexcitation dynamics and the subsequent carrier relaxation processes.

Here we study the charge carriers dynamics in graphene involving a $4 \times 4 \times 1$ supercell. After the graphene sheet is equilibrated by a ground-state RPMD simulation with 12 beads at 50 K, two electrons are excited from an energy level of 3.0 eV below the Fermi level to that of 3.0 eV above the Fermi level, illustrated in Figure 8a. The carrier dynamics is simulated via RP-TDAP method with the microcanonical (NVE) ensemble. With the classical approximation on the nuclear motions, the number of hole occupation in graphene is reduced to half of the initial value within 60 fs (Figure 8b). When applying the quantum description of nuclear motions, strong quantum couplings promote the electron–electron and electron–phonon scatterings, yielding a faster decay of carrier than in the classical nuclear simulation, as shown in Figure 8c. Since different nuclear configurations are sufficiently sampled involving RPMD approach, sufficient sampling of electronic occupation and couplings are also included, resulting in a better description for electron–electron scattering. Fitting to the exponential decay of hole occupation averaged over 12 beads, the relaxation time obtained from the quantum nuclei approach is 14 fs, significantly shorter than 63 fs computed from classical nuclei simulations. In experiment, the energy level of holes is 0.8 eV below the Fermi level,[10] compared to 3.0 eV below the Fermi level found in the present simulations, and thus the calculated life time is expected to be smaller than that in experiment. Evidently, the quantum electronic-nuclear simulations can capture and well depict the ultrafast charge carrier redistribution in graphene observed in experiment, while the imprecise description obtained from classical nuclear simulations may be due to improper treatment of electron–electron and electron–phonon scatterings by the rigid ion approximation.

4 | CONCLUSION

In summary, we develop a set of effective computational approaches based on rt-TDDFT for large scale simulations of excitedstate dynamics. Involving these rt-TDDFT methods we are able to perform time-dependent evolution for both electronic wave functions and ionic movements and trace the real time ultrafast dynamics and phenomena no matter in perturbative or nonperturbative regimes. We derive the TDSCF equations in the presence of external fields from the TDSE, depending on the evolution of electronic wave functions and nuclear coordinates. NAO and PW basis sets have been adopted and implemented to ensure the flexibility and credibility of applying the dynamic approach to diverse systems, including molecules, liquids, solids, interfaces, and low-dimensional materials in various environments.

Furthermore, rt-TDDFT has been combined with RPMD, providing a practical computational scheme to describe both electronic and nuclear dynamics in a quantum manner. The nuclear Hamiltonian is solved using RPMD based on imaginary-time path integral simulations, and the mean field forces exerted on nuclei are calculated within the framework of time-dependent Kohn–Sham orbitals.

We present several examples including studies on HHG, CDW, photocatalysis and NQE, to demonstrate the strength of our approaches, most of which represent a new prospect in their respective areas. The reliability and predictability of methods have been verified by comparing to experimental measurements. These developments and applications represent a significant step towards a full quantum description of electronic and nuclear states from first-principles, to obtain a comprehensive and predictive understanding of quantum interactions and dynamics of complex materials at the atomic and attosecond scale.

ACKNOWLEDGMENTS

We acknowledge helpful discussions with Dr L. Yan, Dr J. Zhang, Dr J.Y. Xu, Dr M.X. Guan, S.Q. Hu, S. J. Zhang, and others, and their contribution to the research described here. We acknowledge financial support from NSFC (Grant Nos. 91850120, 11934003, 11974400, and 11774396), MOST (Grant Nos. 2016YFA0300902 and 2015CB921001), and "Strategic Priority Research Program B" of the CAS (No. XDB330301).

CONFLICT OF INTEREST

The authors have declared no conflicts of interest for this article.

AUTHOR CONTRIBUTIONS

Peiwei You: Formal analysis; writing-original draft. **Daqiang Chen:** Methodology; writing-original draft. **Chao Lian:** Conceptualization; formal analysis; investigation. **Cui Zhang:** Supervision; writing-review and editing. **Sheng Meng:** Conceptualization; funding acquisition; methodology; resources; supervision; writing-original draft; writing-review and editing.

ORCID

Peiwei You https://orcid.org/0000-0003-1606-4810
Sheng Meng https://orcid.org/0000-0002-1553-1432

RELATED WIREs ARTICLES

Semiempirical quantum-chemical methods
Ab initio nonadiabatic molecular dynamics investigations on the excited carriers in condensed matter systems
Excited-state dynamics
Studying molecular quantum dynamics with the multiconfiguration time-dependent Hartree method

REFERENCES

1. Ravetz BD, Pun AB, Churchill EM, Congreve DN, Rovis T, Campos LM. Photoredox catalysis using infrared light via triplet fusion upconversion. *Nature*. 2019;*565*:343–346.
2. Zhang M, de Respinis M, Frei H. Time-resolved observations of water oxidation intermediates on a cobalt oxide nanoparticle catalyst. *Nat Chem*. 2014;*6*:362–367.
3. Wang Q, Hisatomi T, Jia Q, et al. Scalable water splitting on particulate photocatalyst sheets with a solar-to-hydrogen energy conversion efficiency exceeding 1. *Nat Mater*. 2016;*15*:611–615.
4. Ferrari AC. Raman spectroscopy of graphene and graphite: Disorder, electron–phonon coupling, doping and nonadiabatic effects. *Solid State Commun*. 2007;*143*:47–57.
5. Schaller RD, Pietryga JM, Goupalov SV, Petruska MA, Ivanov SA, Klimov VI. Breaking the phonon bottleneck in semiconductor nanocrystals via multiphonon emission induced by intrinsic nonadiabatic interactions. *Phys Rev Lett*. 2005;*95*:196401.
6. Mehlhorn M, Gawronski H, Morgenstern K. Diffusion and dimer formation of CO molecules induced by femtosecond laser pulses. *Phys Rev Lett*. 2010;*104*:076101.
7. Dawlaty JM, Shivaraman S, Chandrashekhar M, Rana F, Spencer MG. Measurement of ultrafast carrier dynamics in epitaxial graphene. *Appl Phys Lett*. 2008;*92*:042116.
8. Nicholson CW, Lücke A, Schmidt WG, et al. Beyond the molecular movie: Dynamics of bands and bonds during a photoinduced phase transition. *Science*. 2018;*362*:821–825.
9. Rohwer T, Hellmann S, Wiesenmayer M, et al. Collapse of long-range charge order tracked by time-resolved photoemission at high momenta. *Nature*. 2011;*471*:490–493.
10. Rohde G, Stange A, Muller A, et al. Ultrafast formation of a Fermi-Dirac distributed electron gas. *Phys Rev Lett*. 2018;*121*:256401.
11. Beck MH, Jäckle A, Worth GA, Meyer HD. The multiconfiguration time-dependent Hartree (MCTDH) method: A highly efficient algorithm for propagating wavepackets. *Phys Rep*. 2000;*324*:1–105.

12. Meyer H-D, Worth GA. Quantum molecular dynamics: Propagating wavepackets and density operators using the multiconfiguration time-dependent Hartree method. *Theoret Chem Accounts*. 2003;*109*:251–267.
13. Richings GW, Polyak I, Spinlove KE, Worth GA, Burghardt I, Lasorne B. Quantum dynamics simulations using Gaussian wavepackets: The vMCG method. *Int Rev Phys Chem*. 2015;*34*:269–308.
14. Curchod BFE, Martinez TJ. Ab initio nonadiabatic quantum molecular dynamics. *Chem Rev*. 2018;*118*:3305–3336.
15. Mac Kernan D, Ciccotti G, Kapral R. Trotter-based simulation of quantum-classical dynamics. *J Phys Chem B*. 2008;*112*:424–432.
16. Kelly A, Markland TE. Efficient and accurate surface hopping for long time nonadiabatic quantum dynamics. *J Chem Phys*. 2013;*139*: 014104.
17. Curchod BF, Tavernelli I, Rothlisberger U. Trajectory-based solution of the nonadiabatic quantum dynamics equations: An on-the-fly approach for molecular dynamics simulations. *Phys Chem Chem Phys*. 2011;*13*:3231–3236.
18. Agostini F, Min SK, Abedi A, Gross EK. Quantum-classical nonadiabatic dynamics: Coupled- vs independent-trajectory methods. *J Chem Theory Comput*. 2016;*12*:2127–2143.
19. Tully JC, Preston RK. Trajectory surface hopping approach to nonadiabatic molecular collisions: The reaction of H+ with D2. *J Chem Phys*. 1971;*55*:562–572.
20. Craig CF, Duncan WR, Prezhdo OV. Trajectory surface hopping in the time-dependent Kohn–Sham approach for electron-nuclear dynamics. *Phys Rev Lett*. 2005;*95*:163001.
21. Tully JC. Mixed quantum–classical dynamics. *Faraday Discuss*. 1998;*110*:407–419.
22. Meng S, Kaxiras E. Real-time, local basis-set implementation of time-dependent density functional theory for excited state dynamics simulations. *J Chem Phys*. 2008;*129*:054110.
23. Bircher MP, Liberatore E, Browning NJ, et al. Nonadiabatic effects in electronic and nuclear dynamics. *Struct Dyn*. 2017;*4*:061510.
24. Meyera HD, Miller WH. A classical analog for electronic degrees of freedom in nonadiabatic collision processes. *J Chem Phys*. 1979;*70*: 3214–3223.
25. Noda M, Sato SA, Hirokawa Y, et al. SALMON: Scalable ab-initio light-matter simulator for optics and nanoscience. *Comput Phys Commun*. 2019;*235*:356–365.
26. K. Dewhurst, S. Sharma, L. Nordström, et al., ELK FP-LAPW code, version 3.3.17 (2016). http://elk.sourceforge.net
27. Andrade X, Alberdi-Rodriguez J, Strubbe DA, et al. Time-dependent density-functional theory in massively parallel computer architectures: The OCTOPUS project. *J Phys Condens Matter*. 2012;*24*:233202.
28. Ojanpera A, Havu V, Lehtovaara L, Puska M. Nonadiabatic Ehrenfest molecular dynamics within the projector augmented-wave method. *J Chem Phys*. 2012;*136*:144103.
29. Mortensen JJ, Hansen LB, Jacobsen KW. Real-space grid implementation of the projector augmented wave method. *Phys Rev B*. 2005; *71*:035109.
30. Dohn AO, Jonsson EO, Levi G, et al. Grid-based projector augmented wave (GPAW) implementation of quantum mechanics/molecular mechanics (QM/MM) electrostatic embedding and application to a solvated diplatinum complex. *J Chem Theory Comput*. 2017;*13*: 6010–6022.
31. Marini A, Hogan C, Grüning M, Varsano D. yambo: An ab initio tool for excited state calculations. *Comput Phys Commun*. 2009;*180*: 1392–1403.
32. Valiev M, Bylaska EJ, Govind N, et al. NWChem: A comprehensive and scalable open-source solution for large scale molecular simulations. *Comput Phys Commun*. 2010;*181*:1477–1489.
33. Lian C, Guan M, Hu S, Zhang J, Meng S. Photoexcitation in solids: First-principles quantum simulations by real-time TDDFT. *Adv Theory Simul*. 2018;*1*:1800055.
34. Craig IR, Manolopoulos DE. Quantum statistics and classical mechanics: Real time correlation functions from ring polymer molecular dynamics. *J Chem Phys*. 2004;*121*:3368–3373.
35. Markland TE, Manolopoulos DE. An efficient ring polymer contraction scheme for imaginary time path integral simulations. *J Chem Phys*. 2008;*129*:024105.
36. You P, Xu J, Lian C, et al. Quantum dynamics simulations: Combining path integral nuclear dynamics and real-time TDDFT. *Electron Struct*. 2019;*1*:044005.
37. Guan M-X, Lian C, Hu S-Q, et al. Cooperative evolution of intraband and interband excitations for high-harmonic generation in strained MoS_2. *Phys Rev B*. 2019;*99*:184306.
38. Zhang J, Lian C, Guan M, et al. Photoexcitation induced quantum dynamics of charge density wave and emergence of a collective mode in 1T-TaS2. *Nano Lett*. 2019;*19*:6027–6034.
39. Lian C, Zhang SJ, Hu SQ, Guan MX, Meng S. Ultrafast charge ordering by self-amplified exciton-phonon dynamics in TiSe2. *Nat commun*. 2020;*11*:43.
40. Yan L, Xu J, Wang F, Meng S. Plasmon-induced ultrafast hydrogen production in liquid water. *J Phys Chem Lett*. 2018;*9*:63–69.
41. Abedi A, Maitra NT, Gross EK. Exact factorization of the time-dependent electron-nuclear wave function. *Phys Rev Lett*. 2010;*105*: 123002.
42. Agostini F, Gross EKU, Curchod BFE. Electron-nuclear entanglement in the time-dependent molecular wavefunction. *Comput Theoret Chem*. 2019;*1151*:99–106.
43. Runge E, Gross EKU. Density-functional theory for time-dependent systems. *Phys Rev Lett*. 1984;*52*:997–1000.

44. Botti S, Schindlmayr A, Sole RD, Reining L. Time-dependent density-functional theory for extended systems. *Rep Prog Phys*. 2007;*70*: 357–407.
45. Sharma S, Dewhurst JK, Sanna A, Gross EKU. Bootstrap approximation for the exchange-correlation kernel of time-dependent density-functional theory. *Phys Rev Lett*. 2011;*107*:186401.
46. Bertsch GF, Iwata JI, Rubio A, Yabana K. Real-space, real-time method for the dielectric function. *Phys Rev B*. 2000;*62*:7998–8002.
47. Yabana K, Nakatsukasa T, Iwata JI, Bertsch GF. Real-time, real-space implementation of the linear response time-dependent density-functional theory. *Phys Status Solidi (b)*. 2006;*243*:1121–1138.
48. Castro A, Marques MA, Rubio A. Propagators for the time-dependent Kohn–Sham equations. *J Chem Phys*. 2004;*121*:3425–3433.
49. Andrade X, Castro A, Zueco D, et al. Modified Ehrenfest formalism for efficient large-scale ab initio molecular dynamics. *J Chem Theory Comput*. 2009;*5*:728–742.
50. Fiedler SL, Eloranta J. Nonadiabatic dynamics by mean-field and surface-hopping approaches: Energy conservation considerations. *Mol Phys*. 2010;*108*:1471–1479.
51. Lan Zhenggang JS. Approximate theoretical methods for nonadiabatic dynamics of polyatomic molecules. *Prog Chem*. 2012;*24*:1105–1119.
52. Parandekar PV, Tully JC. Mixed quantum-classical equilibrium. *J Chem Phys*. 2005;*122*:094102.
53. Hack MD, Wensmann AM, Truhlar DG, Ben-Nun M, Martínez TJ. Comparison of full multiple spawning, trajectory surface hopping, and converged quantum mechanics for electronically nonadiabatic dynamics. *J Chem Phys*. 2001;*115*:1172–1186.
54. Subotnik JE, Jain A, Landry B, Petit A, Ouyang W, Bellonzi N. Understanding the surface hopping view of electronic transitions and decoherence. *Annu Rev Phys Chem*. 2016;*67*:387–417.
55. Dhara AK, Ghosh SK. Density-functional theory for time-dependent systems. *Phys Rev A Gen Phys*. 1987;*35*:442–444.
56. Giannozzi P, Baroni S, Bonini N, et al. QUANTUM ESPRESSO: A modular and open-source software project for quantum simulations of materials. *J Phys Condens Matter*. 2009;*21*:395502.
57. Wang Z, Li SS, Wang LW. Efficient real-time time-dependent density functional theory method and its application to a collision of an ion with a 2D material. *Phys Rev Lett*. 2015;*114*:063004.
58. Ren J, Vukmirović N, Wang L-W. Nonadiabatic molecular dynamics simulation for carrier transport in a pentathiophene butyric acid monolayer. *Phys Rev B*. 2013;*87*:205117.
59. Parrinello M, Rahman A. Study of an F center in molten KCl. *J Chem Phys*. 1984;*80*:860–867.
60. Craig IR, Manolopoulos DE. A refined ring polymer molecular dynamics theory of chemical reaction rates. *J Chem Phys*. 2005;*123*: 34102.
61. Miller TF, Manolopoulos DE. Quantum diffusion in liquid water from ring polymer molecular dynamics. *J Chem Phys*. 2005;*123*: 154504.
62. Ceriotti M, More J, Manolopoulos DE. -PI: A Python interface for ab initio path integral molecular dynamics simulations. *Comput Phys Commun*. 2014;*185*:1019–1026.
63. Kapil V, Rossi M, Marsalek O, et al. -PI 2.0: A universal force engine for advanced molecular simulations. *Comput Phys Commun*. 2019; *236*:214–223.
64. Paul PM, Toma ES, Breger P, et al. Observation of a train of attosecond pulses from high harmonic generation. *Science*. 2001;*292*:1689–1692.
65. Uiberacker M, Uphues T, Schultze M, et al. Attosecond real-time observation of electron tunnelling in atoms. *Nature*. 2007;*446*: 627–632.
66. Cocker TL, Peller D, Yu P, Repp J, Huber R. Tracking the ultrafast motion of a single molecule by femtosecond orbital imaging. *Nature*. 2016;*539*:263–267.
67. Vampa G, McDonald CR, Orlando G, Klug DD, Corkum PB, Brabec T. Theoretical analysis of high-harmonic generation in solids. *Phys Rev Lett*. 2014;*113*:073901.
68. Golde D, Meier T, Koch SW. High harmonics generated in semiconductor nanostructures by the coupled dynamics of optical inter- and intraband excitations. *Phys Rev B*. 2008;*77*:075330.
69. Tancogne-Dejean N, Mucke OD, Kartner FX, Rubio A. Impact of the electronic band structure in high-harmonic generation spectra of solids. *Phys Rev Lett*. 2017;*118*:087403.
70. Perfetti L, Loukakos PA, Lisowski M, et al. Time evolution of the electronic structure of 1T-TaS2 through the insulator-metal transition. *Phys Rev Lett*. 2006;*97*:067402.
71. Eichberger M, Schafer H, Krumova M, et al. Snapshots of cooperative atomic motions in the optical suppression of charge density waves. *Nature*. 2010;*468*:799–802.
72. Hellmann S, Rohwer T, Kallane M, et al. Time-domain classification of charge-density-wave insulators. *Nat Commun*. 2012;*3*:1069.
73. Petersen JC, Kaiser S, Dean N, et al. Clocking the melting transition of charge and lattice order in 1T-TaS2 with ultrafast extreme-ultraviolet angle-resolved photoemission spectroscopy. *Phys Rev Lett*. 2011;*107*:177402.
74. Mohr-Vorobeva E, Johnson SL, Beaud P, et al. Nonthermal melting of a charge density wave in $TiSe_2$. *Phys Rev Lett*. 2011;*107*:036403.
75. Porer M, Leierseder U, Menard JM, et al. Non-thermal separation of electronic and structural orders in a persisting charge density wave. *Nat Mater*. 2014;*13*:857–861.
76. Zou X, Zhang Y. Noble metal-free hydrogen evolution catalysts for water splitting. *Chem Soc Rev*. 2015;*44*:5148–5180.
77. Kudo A, Miseki Y. Heterogeneous photocatalyst materials for water splitting. *Chem Soc Rev*. 2009;*38*:253–278.

78. Maeda K, Domen K. New non-oxide photocatalysts designed for overall water splitting under visible light. *J Phys Chem C*. 2007;*111*: 7851–7861.
79. Fujishima A, Honda K. Electrochemical photolysis of water at a semiconductor electrode. *Nature*. 1972;*238*:37–38.
80. Guo Q, Zhou C, Ma Z, Yang X. Fundamentals of TiO_2 photocatalysis: Concepts, mechanisms, and challenges. *Adv Mater*. 2019;*31*.
81. Wang X, Maeda K, Thomas A, et al. A metal-free polymeric photocatalyst for hydrogen production from water under visible light. *Nat Mater*. 2009;*8*:76–80.
82. Linic S, Christopher P, Ingram DB. Plasmonic-metal nanostructures for efficient conversion of solar to chemical energy. *Nat Mater*. 2011;*10*:911–921.
83. Kibria MG, Chowdhury FA, Zhao S, et al. Visible light-driven efficient overall water splitting using p-type metal-nitride nanowire arrays. *Nat Commun*. 2015;*6*:6797.
84. Liu Z, Hou W, Pavaskar P, Aykol M, Cronin SB. Plasmon resonant enhancement of photocatalytic water splitting under visible illumination. *Nano Lett*. 2011;*11*:1111–1116.
85. Zheng J, Zhang C, Dickson RM. Highly fluorescent, water-soluble, size-tunable gold quantum dots. *Phys Rev Lett*. 2004;*93*:077402.
86. Yan L, Wang F, Meng S. Quantum mode selectivity of plasmon-induced water splitting on gold nanoparticles. *ACS Nano*. 2016;*10*: 5452–5458.
87. Kang JH, Kim DS, Park QH. Local capacitor model for plasmonic electric field enhancement. *Phys Rev Lett*. 2009;*102*:093906.
88. Yan L, Meng S. Atomistic insights into plasmon induced water splitting. *Sci China Phys Mech Astron*. 2017;*60*:027032.
89. Rini M, Magnes B-Z, Pines E, Nibbering ETJ. Real-time observation of bimodal proton transfer in acid–base pairs in water. *Science*. 2003;*301*:349–352.
90. Dai L, Xue Y, Qu L, Choi HJ, Baek JB. Metal-free catalysts for oxygen reduction reaction. *Chem Rev*. 2015;*115*:4823–4892.
91. Liu J, Liu Y, Liu N, et al. Metal-free efficient photocatalyst for stable visible water splitting via a two-electron pathway. *Science*. 2015; *347*:970–974.
92. Jiao Y, Zheng Y, Chen P, Jaroniec M, Qiao SZ. Molecular scaffolding strategy with synergistic active centers to facilitate electrocatalytic CO_2 reduction to hydrocarbon/alcohol. *J Am Chem Soc*. 2017;*139*:18093–18100.
93. Liu G, Niu P, Sun C, et al. Unique electronic structure induced high Photoreactivity of sulfur-doped graphitic C3N4. *J Am Chem Soc*. 2010;*132*:11642–11648.
94. Zhang J, Sun J, Maeda K, et al. Sulfur-mediated synthesis of carbon nitride: Band-gap engineering and improved functions for photocatalysis. *Energ Environ Sci*. 2011;*4*:675–678.
95. Ma H, Feng J, Jin F, Wei M, Liu C, Ma Y. Where do photogenerated holes at the g-C3N4/water interface go for water splitting: H_2O or OH(−)? *Nanoscale*. 2018;*10*:15624–15631.
96. Ren J, Kaxiras E, Meng S. Optical properties of clusters and molecules from real-time time-dependent density functional theory using a self-consistent field. *Mol Phys*. 2010;*108*:1829–1844.
97. Chen JL, Hu WP. Theoretical prediction on the thermal stability of cyclic ozone and strong oxygen tunneling. *J Am Chem Soc*. 2011; *133*:16045–16053.
98. Butscher S, Milde F, Hirtschulz M, Malić E, Knorr A. Hot electron relaxation and phonon dynamics in graphene. *Appl Phys Lett*. 2007; *91*:203103.
99. Lui CH, Mak KF, Shan J, Heinz TF. Ultrafast photoluminescence from graphene. *Phys Rev Lett*. 2010;*105*:127404.
100. Johannsen JC, Ulstrup S, Cilento F, et al. Direct view of hot carrier dynamics in graphene. *Phys Rev Lett*. 2013;*111*:027403.
101. Stange A, Sohrt C, Yang LX, et al. Hot electron cooling in graphite: Supercollision versus hot phonon decay. *Phys Rev B*. 2015;*92*: 184303.

How to cite this article: You P, Chen D, Lian C, Zhang C, Meng S. First-principles dynamics of photoexcited molecules and materials towards a quantum description. *WIREs Comput Mol Sci*. 2021;11:e1492. https://doi.org/10.1002/wcms.1492